Journal of The Electrochemical Society

Surface and Defect Chemistry of Porous $La_{0.6}Sr_{0.4}FeO_{3-\delta}$ Electrodes on Polarized Three-Electrode Cells

Journal of The Electrochemical Society, 2022 **169** 094508

Surface and Defect Chemistry of Porous $La_{0.6}Sr_{0.4}FeO_{3-\delta}$ Electrodes on Polarized Three-Electrode Cells

Andreas Nenning,[1,z] Stefan Reuter,[1] Richard Schlesinger,[1] Harald Summerer,[1] Raffael Ramehsan,[2] Lorenz Lindenthal,[2] Manuel Holzmann,[2] Tobias M. Huber,[1,3] Christoph Rameshan,[2] Jürgen Fleig,[1] and Alexander K. Opitz[1]

[1]*Institute of Chemical Technologies and Analytics, Research Group for Electrochemical Energy Conversion, TU, Wien, Austria*
[2]*Institute of Materials Chemistry, Research Group for Electrocatalysis at Surfaces, TU Wien, Austria*
[3]*Huber Scientific, 1120 Wien, Austria*

Even though solid oxide fuel/electrolysis cells (SOFC/SOEC) are already commercially available, the effect of electrochemical polarization on the electrochemical properties and overpotentials of individual electrodes is largely unexplored. This is partly due to difficulties in separating anode and cathode impedance features and overpotentials of operating fuel cells. For this, we present a novel three-electrode geometry to measure single-electrode impedance spectra and overpotentials in solid oxide cells. With this new design, we characterise polarised porous $La_{0.6}Sr_{0.4}FeO_{3-\delta}$ (LSF) electrodes by simultaneous impedance spectroscopy and ambient pressure XPS measurements. With physically justified equivalent circuit models, we can show how the overpotential-dependent changes in the impedance and XPS spectra are related to oxygen vacancy and electronic point defect concentrations, which deterimine the electrochemical properties. The results are overall in very good agreement with the key findings of several previous studies on the bulk defect chemistry and surface chemistry of LSF. They show for example the exsolution of Fe^0 particles during cathodic polarisation in $H_2 + H_2O$ atmosphere that decrease the polarization resistance by roughly one order of magnitude.
 [DOI: 10.1149/1945-7111/ac908b]

Manuscript submitted May 6, 2022; revised manuscript received August 8, 2022. Published September 20, 2022.

Optimising solid oxide fuel and electrolysis cells (SOFCs and SOECs) requires knowledge of the contributions of anode, electrolyte and cathode to the total polarisation resistance and overpotential. Especially a separation of the contributions from anode and cathode in two-electrode cells is far from trivial due to their usually overlapping impedance features. Hence, symmetrical cells with two identical electrodes in a single chamber configuration are often used to investigate the properties of cathodes and anodes individually. Still, such measurements are restricted to open-circuit voltage (OCV) conditions.[1,2] However, the electrode polarization resistance is typically much larger at OCV than at a typical current density of 200–1000 mA cm^{-2}, e.g. shown for LSM-YSZ cermets.[3] This effect is generally visible in the I–V curves of SOFCs, which usually exhibit a pronounced electrode activation feature at low current density. Accordingly, it is challenging to get information on the contributions of anode, cathode and gas diffusion in full cells under current load. Sophisticated tools and approaches have been developed to quantify these contributions, mostly for state-of-the-art $La_{0.6}Sr_{0.4}Co_{0.2}Fe_{0.8}O_{3-\delta}$ cathodes and Ni-YSZ anodes in anode supported cells.[4–6] However, these models are only valid for specific, often technologically relevant cell types, but they cannot be straightforwardly transferred to other electrode materials with different electrochemical properties.

In this study, we overcome these limitations with a novel three-electrode model cell design in which the reference electrode is located on a protrusion at the edge of the electrolyte ("wing" design), which enable virtually artefact-free determination of half-cell impedance spectra and overpotentials, even for electrodes with low polarisation resistance and at technologically relevant current densities.

To gain operando information on the surface chemistry during polarisation, we performed simultaneous ambient pressure X-ray photoelectron spectroscopy (APXPS) and DC-polarized impedance measurements on such a three-electrode cell.

As electrode material, the mixed ion and electron conductor $La_{0.6}Sr_{0.4}FeO_{3-\delta}$ (LSF) was chosen. LSF is chemically similar to the widely used cathode material $La_{0.6}Sr_{0.4}Co_{0.2}Fe_{0.8}O_{3-\delta}$ (LSCF). Due to its cobalt-free composition, it is stable in oxidising and moderately reducing conditions.[7] Moreover, its $p(O_2)$ dependent defect chemistry was already thoroughly investigated by thermogravimetry[7] and chemical capacitance measurements.[8] Mechanistic information on the electrochemical oxygen exchange in oxidising and reducing conditions is available from thin-film electrodes.[9–15]

Due to this, LSF is an excellent model material to verify the strength of our novel three-electrode design, and demonstrate how the electrode overpotential drastically changes the electrochemical properties and surface kinetics of the LSF electrode.[10,13,16]

Point Defect Chemistry and Electrochemical Properties of LSF

The well-investigated point defect chemistry of LSF, which governs the electrochemical properties of the material is a key point in the discussion of the results. LSF is a doped form of $LaFeO_3$ in which 40% of the La^{3+} ions are replaced by Sr^{2+},[7,17] The thereby introduced lack of positive charges is compensated mostly by electronic holes in oxidizing conditions and primarily by oxygen vacancies below 0.1 mbar oxygen partial pressure at 600 °C. In reducing atmospheres, the electronic conduction mechanism changes from hole to electron conductivity, where the electronic charge carriers are localized in form of small polarons at Fe^{2+} ions.[7,10]

For the further discussion of the point defects, we will use Kröger-Vink notation.[18] The most important point defects in LSF are Sr dopants (Sr'_{La}), oxygen vacancies ($V_o^{\cdot\cdot}$), electron holes and reduced Fe^{2+} ions (Fe'_{Fe}). In literature, the exact nature of electron holes is controversially discussed. These are partially considered as delocalized electron holes ($h^{\cdot}$), or as localized carriers in form of Fe^{4+} ($Fe^{\cdot}_{Fe}$) ions, or O^- (O_O) ions. Although the electronic conductivity of LSF exceeds 100 S cm^{-1} in air at 600 °C,[19,20] the electronic structure is not metallic, and no states are occupied at the Fermi level,[10,21] which indicates that the charge carriers are somewhat self-confined in polaronic states.[22] Spectroscopic measurements reveal that the electron hole is more associated to oxygen anions than Fe cations.[21,23] Due to these observations, we consider that the electron holes are best approximated with the model of a polaronic electron hole located at an O^- anion ($O^{\cdot}_O$) in Kröger-Vink notation.

[z]E-mail: andreas.nenning@tuwien.ac.at

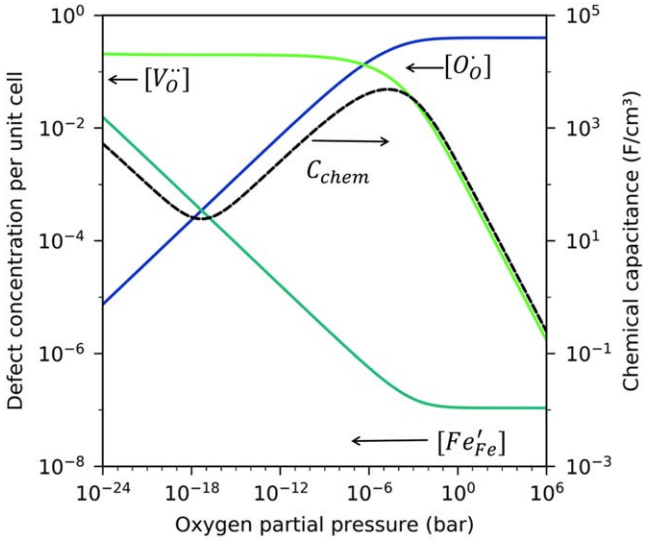

Figure 1. Brouwer diagram of LSF at 600 °C, adapted from Ref. 17 with permission from the author.

The Sr concentration is fixed by extrinsic doping ($[Sr'_{La}] = 0.4$ p.f.u.), whereas the other defect concentrations depend on the $p(O_2)$ and temperature. All concentrations are given as average concentration per ABO_3 formula unit. The concentrations of electron holes, Fe^{2+} ions and oxygen vacancies must obey the charge neutrality condition, given by

$$[O_O^{\cdot}] + 2[V_O^{\cdot\cdot}] = [Sr'_{La}] + [Fe'_{Fe}]. \quad [1]$$

Furthermore, the oxygen exchange equilibrium is given by

$$\frac{1}{2}O_2 + O_O^{\times} + V_O^{\cdot\cdot} \rightleftharpoons 2O_O^{\cdot}. \quad [2]$$

Lastly, the "electron-hole pair" creation equilibrium must be considered, in form of

$$O_O^{\times} + Fe_{Fe}^{\times} \rightleftharpoons O_O^{\cdot} + Fe'_{Fe} \quad [3]$$

In Ref. 7 the equilibrium constants of these defect reactions were determined experimentally, and this data set was used to calculate the Brouwer diagram of LSF at 600 °C, shown in Fig. 1. In electrochemical impedance measurements, the capacitance in parallel to the electrode polarization resistance is the electrode's chemical capacitance. This capacitance is directly proportional to the first derivative of the oxygen vacancy concentration in the Brouwer diagram, or in other words a measure for how much the oxygen vacancy concentration changes with the electrochemical overpotential, or oxygen chemical potential. For dilute, interaction-free point defects, the chemical capacitance is also a function of point defect concentrations, given by[8]

$$C_{chem} = -\frac{4F^2}{RTV_m}\left(\frac{1}{[V_O^{\cdot\cdot}]} + \frac{4}{[O_O^{\cdot}] + [Fe'_{Fe}]}\right)^{-1}. \quad [4]$$

Therein, F is Faraday's constant, T the temperature, R the universal gas constant, T the temperature and V_m is the molar volume of LSF. The resulting s-shaped $p(O_2)$ dependence of the chemical capacitance is shown in Fig. 1 (black curve).

When LSF gets strongly reduced, either in weakly humidified hydrogen or during H_2O electrolysis, a fraction of the Fe B-site ions forms Fe^0 nanoparticles that accelerate the water electrolysis reaction.[10,13,24,25] This catalytic effect of the Fe^0 particles was also investigated on our three-electrode cells.

A Critical Discussion of Three-Electrode Designs

Current efforts in three-electrode impedance.—Three electrode measuremetns are considered as standard in liquid electrochemistry and battery research. However, the lower conductivity and the technical limitations regarding the shaping of solid electrolytes make the realization of three-electrode cells that produce artefact-free half-cell date very demanding. For example, in cells with liquid electrolytes the RE is often a simple thin wire, which is placed between WE and CE without significantly affecting the current distribution.[26,27] This is obviously not possible in a solid electrolyte. Many designs of three-electrode cells were suggested and partly experimentally applied. S.B. Adler critically assessed co-planar three-electrode deisgns,[28] or Cimenti et al.[29,30] and Winkler et al.[31] performed FEM simulations on variously shaped three-electrode cells. However, to the authors' best knowledge, very few studies[32,33] report three-electrode impedance measurements on SOFC electrodes at current densities or overpotentials that are typical for application. Moreover, such studies often use cell designs that were previously classified as extremely prone to artefacts by FEM simulations, and many of the suggested geometries were not experimentally tested—partly because they are very complex to fabricate. Most experimental studies use co-planar electrodes on a thin electrolyte, which are very prone to artifacts by minor alignment errors. To reduce this issue, Stodolny et al.[33] used laser machining of the electrode edges in order to minimize the alignment errors.

Prerequisites for working—and counter electrode impedance separation.—However, even with perfectly aligned WE and CE, artifact features may appear in the impedance spectra, when primary (high frequency, electrolyte-limited) and secondary (low-frequency, electrode-limited) current distributions differ, and the two electrodes have different relaxation frequencies.[28,34] In a literature survey, supplemented by own finite-element simulations of impedance spectra with COMSOL software, we explored artifacts in different three-electrode cell designs.[34] Those show that the geometry and current distributions at the working electrode (WE), counter electrode (CE) and reference electrode (RE) need to fulfill several criteria to acquire artefact-free half-cell impedance spectra. Specifically, those are:

1. Uniform current density at the WE.
2. Identical primary (high frequency, electrolyte dominated) and secondary (low frequency, electrode dominated) current distributions.
3. The reference electrode shall have no influence on the primary and secondary current distributions.
4. If the RE is not placed between WE and CE, the alignment of these two electrodes needs to be very precise.
5. The impedance of the reference electrode must be much smaller than the analyzer input impedance at all frequencies.

These requirements already give several limitations to the model cell design. Requirement 1 and 2 are relatively easy to solve by using a classical cell design with co-planar working and counter electrodes. There, exact alignment of both electrodes is crucial and not trivial to achieve.[28,30,33] However, even with perfectly aligned WE and CE, artifact features may appear in the impedance spectra, when primary (high frequency, electrolyte-limited) and secondary (low-frequency, electrode-limited) current distributions differ, and the two electrodes have different relaxation frequencies.[28,34] Such artifacts are unavoidable, due to the inhomogeneous current at the edges, which is shown in Figs. 2a–2b.

An easy to fabricate and virtually distortion-free three-electrode cell design.—However, when WE and CE are applied on the entire substrate surface, the alienment error is minimal since manufacturing of the electrolyte sheet is more precise than screen printing. Moreover, extending the electrode area to the electrolyte edges

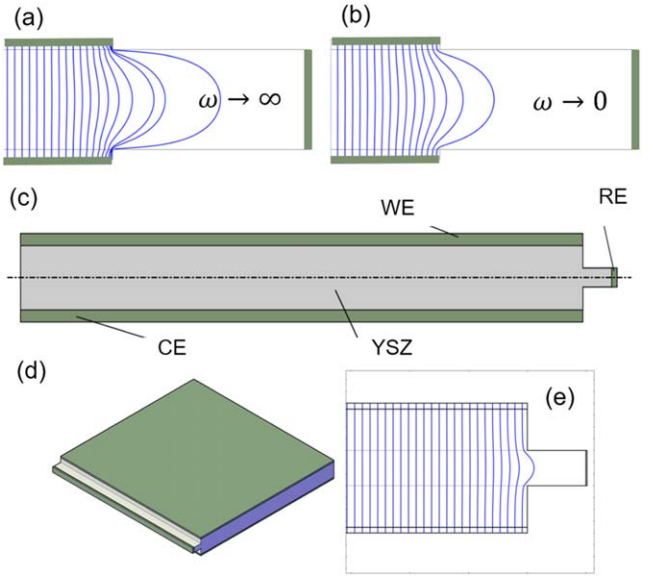

Figure 2. (a)–(b) Primary and secondary current distributions on cells with co-planar electrodes. (c)–(d) Sketch of the "wing" geometry. (e) Simulated uniform current density through the "wing" electrolyte.

ensures an even current distribution at the WE and CE, with equal primary and secondary current distributions (see Fig. 2e). Proper application of a reference electrode on such a co-planar WE and RE geometry is possible by shaping the electrolyte in a new "wing" cell design, which is suggested and applied in this paper. Therein, the reference electrode sits on a protrusion at the edge of the electrolyte, as shown in Fig. 2. As depicted in Fig. 2c, the simulated current distribution is only minimally distorted by the protrusion and the reference electrode, so this design also fulfils requirements 3 and 4.

Nonetheless, even with the "wing" design tiny distortions may appear, when the CE impedance is relatively large. In Fig. 3, simulated impedance spectra are shown. For increasing the artifact amplitude, a large CE polarization resistance (5 Ωcm^2) and small WE resistance (0.5 Ωcm^2) was chosen. When furthermore the WE and CE relaxation frequencies differ (Fig. 3b), a small artifact loop becomes visible. Noteworthy, this artifact feature diameter is less than 1% of the CE polarization resistance.

Also requirement no. 5 is a common source of artefacts. Although the DC input bias current at the RE terminal of most impedance analyzers is negligibly low (ca 10^{-12} A), the capacitance of the input amplifier (ca 25 pF) and the capacitance of the coaxial wire that is connected to the RE (ca 100 pF m^{-1}) can cause problems at high frequencies.[34] At 1 MHz, the capacitive impedance of the wires and input amplifier is in the order of 2000 Ω. In our case, this value is not much larger than the impedance of the reference electrode (500–1000 Ω), so the reference electrode potential in the high frequency limit may deviate from its open circuit potential. This problem can be minimized through increasing the RE area (so the RE polarization resistance decreases), minimizing the wire length and active shielding of the RE wire. For the cells used in this study, the electrochemical electrode features all have characteristic frequencies <1000 Hz, and hence the capacitive RE input impedance is $>10^6$ Ω. Thus, the artifact features therefore have no frequency overlap with the electrode impedance.

Experimental

Fabrication of the three-electrode cells.—Single-crystalline "wing" design YSZ electrolytes were fabricated on demand by CrysTec GmbH, Germany. The electrolyte dimensions were $5 \times 5 \times 1$ mm^3, with a 0.4 mm long and 0.3 mm wide protrusion at one of the edges. On these electrolytes, different electrode pastes were applied either by screen printing (for ca. 10 μm thick layers) or

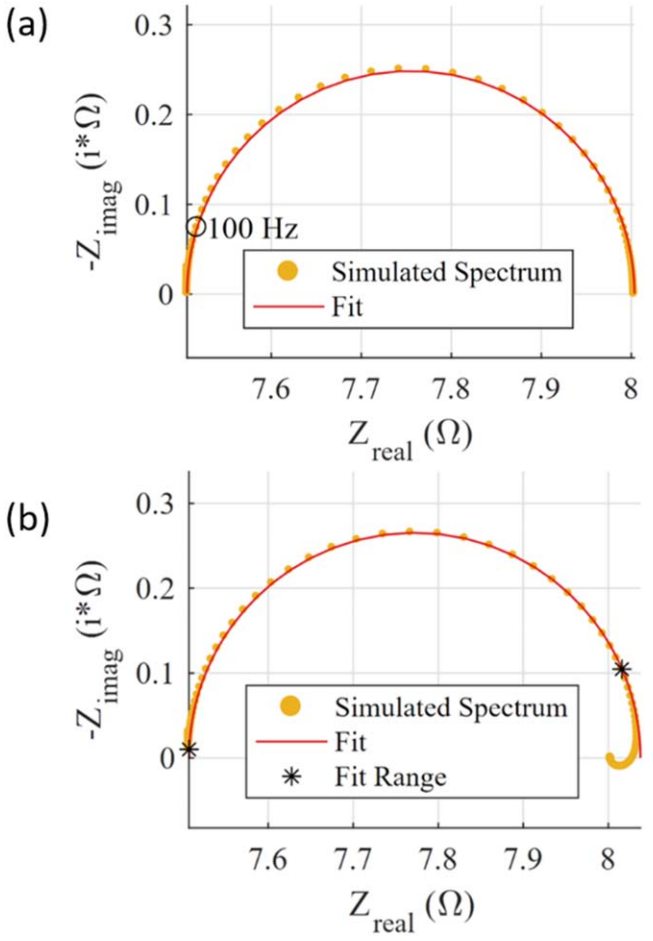

Figure 3. Simulated WE half-cell impedance spectra for the "wing" geometry with asymmetric electrodes ($R_{pol}(CE) = 10*R_{pol}(WE)$) and (a) equal CE summit frequency, and (b) slower CE summit frequency.

by spin-coating of electrode pastes (for 3–4 μm thick layers). The reference electrode consisted of the counter electrode material (either Pt-YSZ cermet, or a bilayer of GDC|Pt), and was applied with a fine brush under a microscope. The advantages of these RE materials compared to the conventionally used Pt particle paste are lower polarization resistance (more stable RE potential) and better adhesion to the YSZ substrate.

Different particle suspensions were used as inks for electrode preparation: Pt and Pt-YSZ pastes were used as sold from the supplier (TR-7907 and TR-706P4, Tanaka Japan). The GDC, LSF and Pt-GDC electrode pastes were prepared by mixing the oxide powders with a terpineol based ink vehicle (FuelCellMaterials, USA) in a mass ratio of 1:1. For the powders we used the following suppliers: $La_{0.6}Sr_{0.4}FeO_3$ (LSF) powder from Sigma Aldrich (500 nm particle size), $Ce_{0.9}Gd_{0.1}O_{1.95}$ (GDC, 270 nm particle size) from Treibacher, Austria and platinum particles from Tanaka, product name AY-1050.

The first generation of cells was used for EIS measurements only. Those were fabricated as follows: Counter and reference electrodes consisting of Pt-YSZ cermet were prepared by brushing a 10 μm thick layer of commercial Pt-YSZ paste, followed by sintering at 1350 °C for 1 h in air. On the WE side of the cell, first a 400 nm thick, dense GDC buffer layer was deposited by pulsed laser deposition (PLD) with a KrF excimer laser at a pulse energy of 100 mJ, substrate temperature of 600 °C and 0.04 mbar O_2 atmosphere. Subsequently, the 10 μm thick LSF layer was screen printed and dried, and Pt paste as current collector was brushed on top. Both layers were co-sintered for 3 h at 1050 °C in air, with the resulting cell sketched in Fig. 4a. These

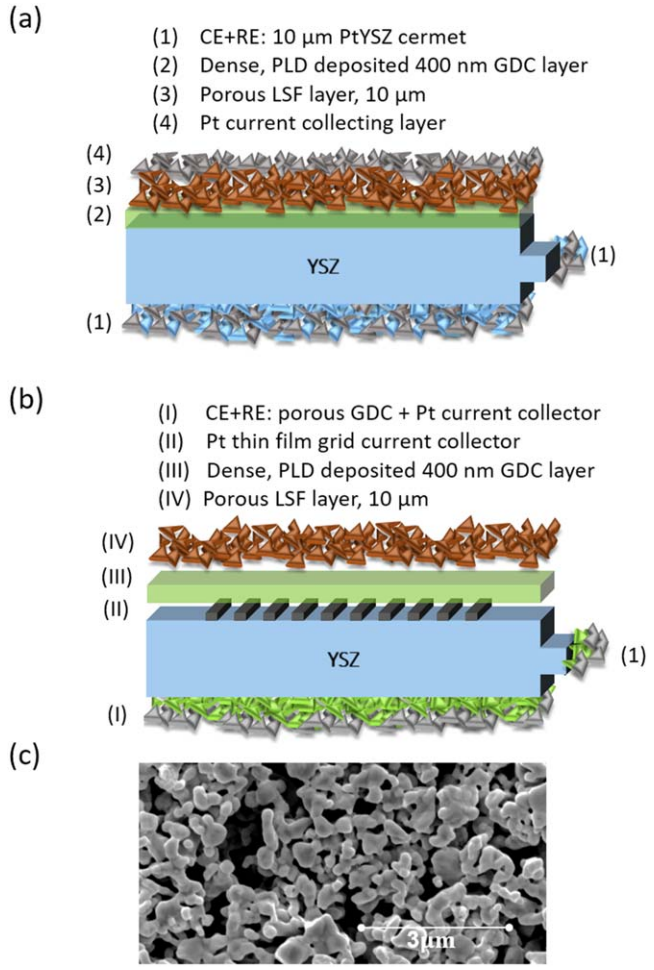

Figure 4. (a) Design of the model cells for 3-electrode impedance measurements. (b) Model cell for combined APXPS + impedance measurements, (c) top-view SEM image of the LSF surface of cell (b).

cells were then electrochemically characterized in the single chamber three-electrode electrochemical testing equipment pictured in Fig. 5a.

A second generation of cells was used for combined EIS and APXPS measurements. Those were based on the same 5 × 5 × 1 mm^3 "wing" shaped electrolytes, but had a more optimized counter electrode with faster kinetics in reducing H_2 + H_2O atmospheres. The 2nd generation CE was prepared by spin-coating of a 3 μm thick GDC layer, followed by drying at 120 °C and subsequent brushing of a Pt-GDC cermet and a pure Pt layer for current collection. Subsequently, the three layers (GDC, Pt-GDC and Pt) were sintered in one step at 1150 °C for 3 h in air. Details on the preparation and performance of the counter electrode are given in Ref. 35. In addition, the working electrode of these cells was prepared differently. In order to have a surface that is accessible to APXPS investigation, the current collection layer was prepared as a sputtered Ti/Pt thin film grid (5 nm Ti + 150 nm Pt), which was structured by photolithography and subsequent Ar-ion beam etching. The 400 nm thick GDC buffer layer was deposited by pulsed laser deposition (PLD) on top of the Pt grid at 600 °C in 0.04 mbar O_2. In this case, the buffer layer not only prevents a reaction between LSF and YSZ, but also stabilizes the Pt grid against dewetting during the sintering step. The LSF functional layer on these cells was applied by slurry spin coating and sintered at 1000 °C for 3 h in air, resulting in a 4 μm thick porous LSF film. The cell design is sketched in Fig. 4b, a top view SEM picture of the LSF microstructure is shown in Fig. 4c.

Electrochemical impedance characterization.—For electrochemical characterization, the samples were mounted in a homogeneously

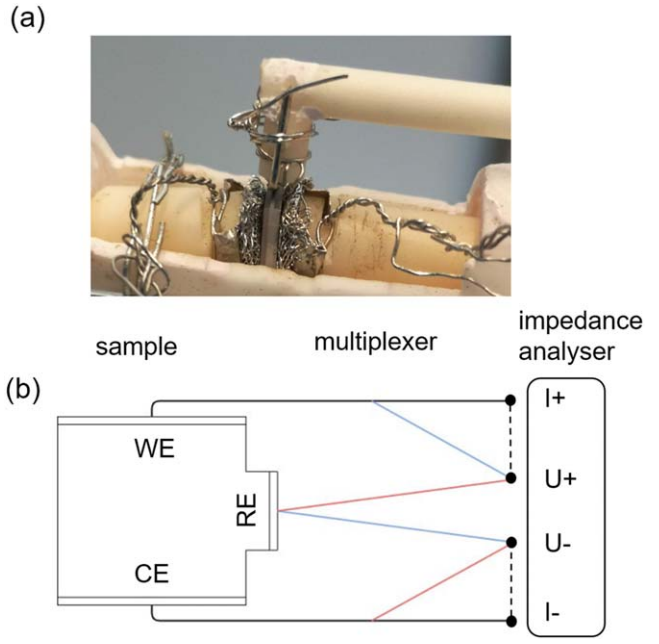

Figure 5. (a) Image of a three-electrode sample electrically contacted in the dedicated testing chamber. The Pt wire mounted on top of the sample contacts the RE. (b) Sketch of the wiring between the sample electrodes and the impedance analyzer. The wiring in the WE half-cell configuration is sketched with blue lines, the CE half-cell configuration with red lines.

heated testing setup in O_2:N_2 mixtures, or in diluted H_2:H_2O mixtures with Ar balance gas. The setup consists of a gas-tight fused silica tube inside a tubular furnace, which is capable of heating the sample up to 900 °C. The mounting and electrical contacting was established through a specialized equipment consisting of alumina and Pt, and a mounted three-electrode cell is shown in Fig. 5a. Impedance measurements were carried out with a Novocontrol Alpha impedance analyser, equipped with a four-wire Pot/Gal 30 V/2 A interface (both Novocontrol GmbH, Germany). Working and counter electrode half-cell impedance spectra were acquired by changing the wiring of the voltage sensing (U + and U-) impedance analyzer terminals, as sketched in Fig. 5b. On the impedance analyzer interface, the positive active terminal is called I+. This was connected to the WE of the model cell, and the grounded current-sensing terminal I- was connected to the CE. In order to measure the WE half cell spectrum, the positive U + terminal was connected to the WE, and the negative reference (U-) terminal was connected to the wing reference electrode. Through an automated multiplexing setup, it was possible to switch between full cell, WE half-cell and CE half-cell measurement, as sketched in Fig. 5b. Impedance spectra were recorded on the different cell types in a frequency range of 10 mHz − 1 MHZ and with an AC amplitude of 20 mV. For these measurements, the temperature was varied between 500 °C and 800 °C in various atmospheres and at a DC bias of −2 V to +2 V. Noteworthy, the largest portion of the DC bias was dropping at the ohmic resistor of the electrolyte, due to its rather high thickness of 1 mm.

Equivalent circuit fitting of impedance measurements.—The half-cell impedance measurements were fitted by a transmission-line type equivalent circuit model, which is conceptually based on the Adler-Lane-Steele model.[2] The mathematical proof of its mechanistic correctness was already elaborated in Ref. 1. A key strength of this model is the possibility to determine the effective ionic conductivity of the porous structure and get information on the defect chemistry of the mixed conducting electrode material from the chemical capacitance.[8,17] The model takes into account the resistances and capacitances associated with ion conduction across the electrode (R_{ion}), electron conduction across the electrode (R_{eon}),

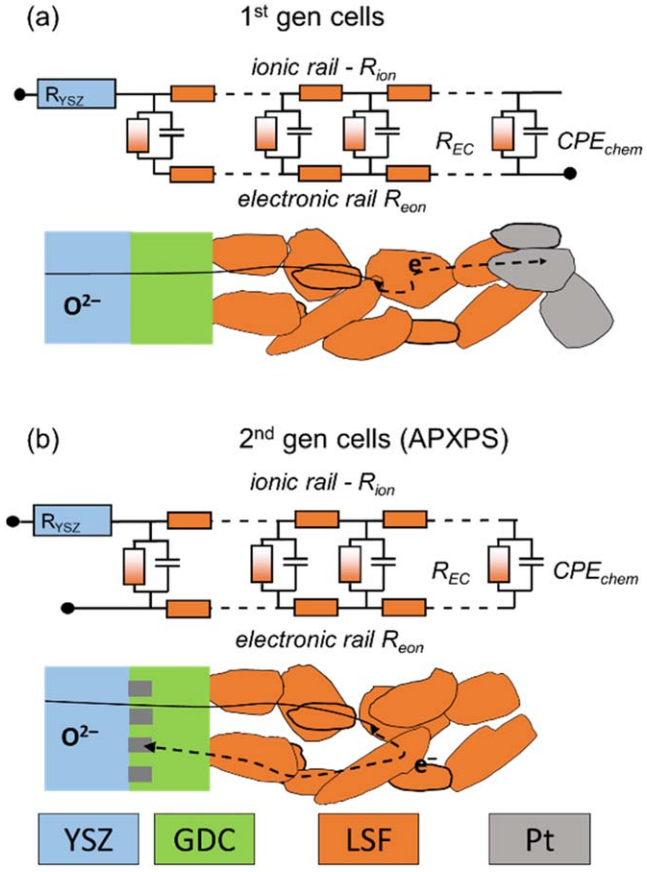

Figure 6. Sketch of the electron and ion conduction pathways in porous LSF electrodes and corresponding equivalent circuits for (a) 1st generation cells (impedance spectroscopy only) and (b) 2nd generation cells (APXPS).

oxygen stoichiometry changes through the chemical capacitance (C_{chem}), and the rate of oxygen exchange at the MIEC surface (R_{EC}).

In principle, also the surface of the GDC diffusion barrier, and the Pt-LSF triple-phase boundary could act as additional sites for oxygen reduction and hydrogen oxidation. However, the polarization resistance of GDC thin film electrodes after some thermal annealing time,[36] and that of a pure Pt particle electrode (with the powder used in this study)[35] are quite large, so that these additional catalytic pathways most likely play a negligible role.

The cells for EIS characterization had the current collector on top of the LSF layer, whereas the current collecting layer of the cells for APXPS characterization was deposited below the active layer. This leads to slightly different electron current pathways that are sketched in Fig. 6. Since LSF is a rather poor electron conductor in reducing atmospheres,[11] this has a slight effect on the mechanistically correct impedance function and the interpretation of the spectra. The ion and electron conduction pathways are sketched in Fig. 6—while the ion conduction pathway is independent on the current collector position, the electron conduction pathways differ.

For the electrode with top current collector (1st generation electrode) the general impedance function is given by.[37]

$$Z = \frac{1}{A_{el}}\left(\frac{R_{ion}R_{eon}}{R_{ion}+R_{eon}}\left(\mathrm{L} + \frac{2\lambda}{\sinh\left(\frac{\mathrm{L}}{\lambda}\right)}\right) + \lambda\frac{(R_{ion}^2+R_{eon}^2)}{R_{ion}+R_{eon}}\coth\left(\frac{L}{\lambda}\right)\right). \quad [5]$$

There, A_{el} is the electrode area, L is the thickness of the porous electrode, R_{ion} and R_{eon} are the inverse of effective ionic and electronic conductivities, and λ is a measure for the characteristic length of the electrochemically polarized zone, expressed by:

$$\lambda = \sqrt{\frac{1}{\left(\frac{1}{R_{EC}} + i\omega C_{chem,eff}\right)(R_{\mathrm{ion}} + R_{eon})}}. \quad [6]$$

For measurements in oxidizing conditions, the electronic conductivity of LSF is relatively high (20–300 S cm^{-1}),[20] so the resistance of electron conduction (R_{con}) is negligible. In this case, the impedance function is simplified to

$$Z = \lambda R_{ion}\coth\left(\frac{L}{\lambda}\right). \quad [7]$$

Also for the cells with embedded thin film current collector (2nd generation cells used for APXPS, Fig. 6b), the impedance function is given by 7—even when the electronic conductivity of LSF becomes low (e.g. in weakly reducing atmospheres). Consequently, only the sum of electron and ion conduction resistance influences the electrode impedance. For fitting, the commercial software "Zview" was used, in which the corresponding impedance functions are implemented by the distributed element titled 'Bisquert#2'.[1]

Ambient-pressure XPS measurements.—Ambient pressure XPS measurements were carried out in a lab-based machine with monochromated Al K_α radiation (μFOCUS 500 NAP, SPECS, Germany) at a total gas phase pressure of 1 mbar. The machine is further equipped with a differentially pumped hemispherical electron energy analyzer (PHOIBOS 150 NAP, SPECS, Germany), which has a water-cooled nozzle. The three-electrode model cells were mounted on a specialized sample stage for high temperature solid state electrochemistry (Huber Scientific, Austria). Details regarding the sample stage can be found in Ref. 38. The sample is mounted on a Pt-coated Al_2O_3 disk with a 4.5 × 4.5 mm^2 central hole on which the 5 × 5 × 1 mm^3 large model cell is positioned. This enables direct sample heating with the near-infrared laser, as sketched in Fig. 7. The GDC|Pt-GDC|Pt counter electrode was contacted by a thin Pt wire on the sample stage. Reference and working electrodes were electrically contacted by Pt-Ir alloy needles—see Fig. 6b. For the WE contact, the needles scratched through the electrode oxide layer, and directly contacted the Pt current collector, which was verified by measuring the resistance between the three contact needles on the WE at room temperature, which was in the order of 10–20 Ω. In order to avoid XPS peak shifts due to the applied voltage, the working electrode was grounded and bias was applied to the counter electrode.

The temperature of the sample was controlled by means of the high frequency resistance in impedance measurements, which stems primarily from ion conduction in the YSZ electrolyte. Due to the thermal activation of the YSZ conductivity,[39] a quite precise (±5 °C) temperature reading of the model cell is possible with this method.

Results and Discussion

Separation of half-cell impedance spectra.—Our experiments have shown that even for our optimized three-electrode cells, the artefact-free separation of WE and CE impedance spectra and overpotentials is only possible when the impedance of the CE is not much larger than that of the WE. For the 1st generation cells, WE and CE half-cell impedance spectra collected at 700 °C in 10 mbar O_2 are shown in Fig. 8a. Clearly visible, the impedance arc of the Pt-YSZ CE is much smaller and has a quite high peak frequency of ca. 4 kHz. This spectrum contains a large inductive artefact feature with a summit frequency that matches the summit frequency of the LSF working electrode at ca. 0.25 Hz. In contrast to the Pt-YSZ half-cell spectra, the LSF half-cell spectra only have a tiny artefact loop feature, which is visible in the inset.

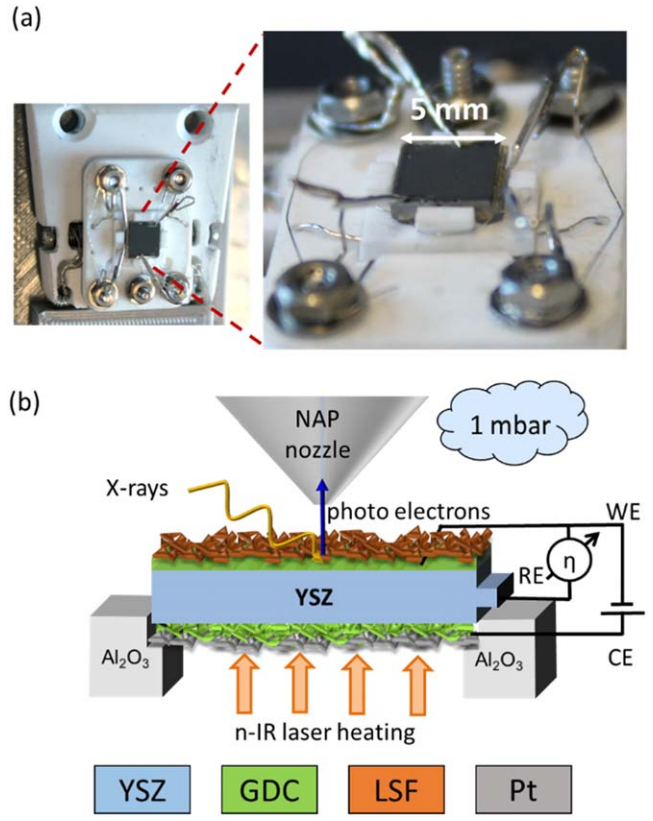

Figure 7. (a) Photographs of the three-electrode cell mounted on the APXPS sample holder. (b) Sketch of the experiment with the 2nd generation cell electrically contacted within the APXPS analyzer.

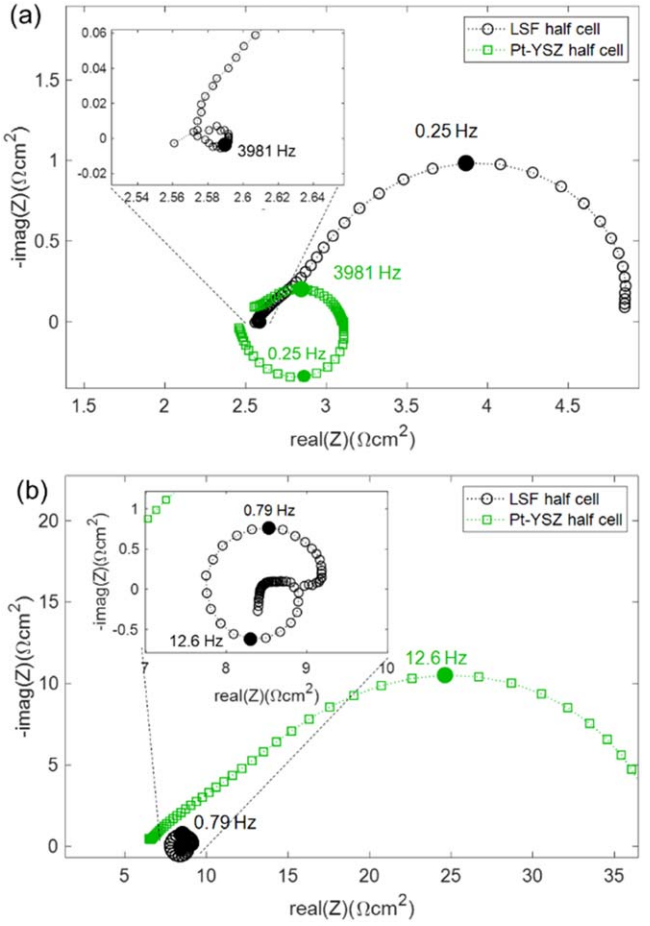

Figure 8. Impedance spectra of the LSF and Pt-YSZ half cells in (a) 10 mbar O_2 at 700 °C and (b) 25 mbar H_2 + 25 mbar H_2O at 600 °C.

In contrast to the almost artefact-free LSF half-cell impedance spectra in 10 mbar O_2, no reasonable measurements of the LSF electrode are possible in reducing atmospheres, which are shown in Fig. 8b. In both oxidizing and reducing conditions, the size of the artefact loop in the LSF spectrum is roughly 3% of the Pt-YSZ counter electrode polarization resistance (slightly larger than the ∼1% that were expected from idealized FEM simulations). The corresponding artifact feature is tiny in oxidizing conditions and very large in reducing conditions, due to the large Pt-YSZ counter electrode impedance in reducing atmospheres. Consequently, a counter electrode with lower polarization resistance is needed in reducing atmospheres.

From these measurements, FEM simulations of ideal "wing" electrolyte designs[34] and previous less successful tests[40] we conclude that the counter electrode always introduces at least minor distortions in the WE impedance, which are proportional to the CE polarization resistance—and can therefore be minimized by usage of a kinetically fast counter electrode. Also, these artefacts always have the same characteristic frequency as the counter electrode. Hence, only when the peak frequencies of WE and CE deviate significantly, artefact features (e.g. due to partial delamination, inhomogeneous electrodes or misalignment) are clearly separated and become obvious. In symmetrical cells, however, artefact features therefore may be "hidden" in form of distorted impedance arcs of the electrodes and lead to qualitatively wrong conclusions. Hence, even for the most advanced three-electrode cell designs, care has to be taken in order to avoid misinterpretations of spectra or fit results.

p(O_2) and bias dependence of the electrochemical properties—cell type 1.—As shown above, for the first generation cells with Pt-YSZ counter electrode, reasonable LSF half-cell impedance measurements were possible in oxidizing atmosphere. One cell was thus investigated by EIS in various oxygen containing gas mixtures and open circuit conditinos, and at varying cathodic and anodic overpotentials in 1% O_2 in N_2.

Resulting LSF half-cell spectra for different p(O_2) values and overpotentials are shown in 8a. The absence of a well-separated high-frequency semicircle indicates that ion conduction through the electrode-electrolyte interface does not cause any observable contribution to the impedance, indicating that the dense GDC film buffer layer effectively prevents the formation of a weakly conductive $La_2Zr_2O_7$ phase.[1,41] Also, all spectra show a 45° slope in the HF region, which is larger for spectra at higher p(O_2) or with anodic polarization. The impedance spectra were fitted to the finite-length transmission line equivalent circuit model[42] shown in Fig. 6a, with the impedance function given in Eq. 5. This model is closely related to the Adler-Lane-Steele model[2]. In this physically motivated circuit model, the resistance associated with electrochemical oxygen exchange on the electrode surface (R_{EC}), effective ionic conductivity ($\sigma_{ion,eff}$) and chemical capacitance (C_{chem}) are fitting parameters, while the electron conduction resistance in across-plane direction (R_{eon}) is negligible due to the reasonably high electron conductivity of LSF in oxidizing atmosphere.[20] The slightly depressed shape of the impedance arcs, was parametrized by using a constant phase element (CPE_{chem}) instead of a capacitor for modelling of the chemical capacitance.

In Fig. 9b, the p(O_2) and overpotential-dependent area-specific resistance (diameter of the electrode arc) is shown. The chemical capacitance (C_{chem}), calculated from the fitting parameters of the parallel CPE_{chem} and R_{EC} elements,[43] and the effective ionic conductivity ($\sigma_{ion,eff} = 1/R_{ion}$) are plotted together in Fig. 9c. For both figures, the overpotential plotted at the upper *x*-axis is linked to

the $p(O_2)$ axis. For rate-limiting surface oxygen exchange at the LSF surface, the overpotential changes the effective oxygen partial pressure $p(O_2)_{eff}$ in the electrode, which defines the oxygen stoichiometry, according to Nernst's equation, given by

$$p(O_2)_{eff} = p(O_2)_{gas} * e^{\frac{4F\eta}{RT}}. \quad [8]$$

The overpotential-dependent measurements were carried out in 0.01 bar O_2, so the equation linking both x-axes is given by

$$\eta = \frac{RT}{4F} \ln\left(\frac{p(O_2)_{eff}}{0.01\ bar}\right). \quad [9]$$

The overpotential η is calculated by subtracting the ohmic electrolyte losses from the voltage between WE and RE

$$\eta = U_{WE-RE} - I_{DC} * R_{YSZ}. \quad [10]$$

Consequently oxygen partial pressure changes and application of an overpotential should have analodougs effects on the chemical capacitance and MIEC properties.[17]

According to the well-investigated defect chemistry of LSF,[7,17,20] which was summarized in the introduction, the amount of oxygen vacancies ($_\delta$) scales with $p(O_2)^{-0.5}$ in the pressure range of 10^{-3}–10^{1} bar, and converges towards a constant value of $_\delta = 0.2$ in the pressure range below 10^{-5} bar. Consequently, the ionic conductivity hould increase monotonically in more reducing conditions, whereas the chemical capacitance should have a maximum at 10^{-4} bar.[17] As shown in Fig. 9c, both expectations are indeed met. Another equally important result is that the fitting parameters shown in Fig. 9c obtained from variation of the gas phase $p(O_2)$ (black symbols) and variation of the overpotential (red symbols) are in good agreement, showing that Eq. 8 is indeed well-suited to describe for the $p(O_2)_{eff}$ within the LSF electrode material. Slight discrepancies from this model are expected, because in Eqs. 8–10 we assume a homogeneous polarization of the entire electrode. In good approximation this is the case as long as the resistance of the oxygen exchange reaction (R_{EC}) is much larger than that of oxygen ion transport within the electrode (R_{ion}). Impedance simulations show that the ion conduction resistance scales linearly with the size of the 45° feature in the spectra. As long as this feature is small compared to the low-frequency semicircle (which scales with R_{EC}), the stoichiometric polarization of the LSF electrode is rather homogeneous. In our measurements, this is the case for $p(O_{2,eff})$ below ca. 200 mbar. In contrast to the ionic conductivity and chemical capacitance, the rate of surface reactions depends on both bulk defect chemistry and gas phase $p(O_2)$. Therefore, the clearly differing ASR values at the same $p(O_2)_{eff}$ shown in Fig. 9b are expected and highlight the importance of the gas phase adsorbate concentrations and the rate of gas phase oxygen molecule collisions for surface kinetics.

p(O₂) and bias dependence of the electrochemical properties—cell type 2.—For also investigating the bias-dependent electrochemical properties of porous LSF electrodes under reducing conditions, a $Ce_{0.9}Gd_{0.1}O_{2-\delta}$ (GDC)-based counter electrode with excellent kinetics in oxidizing and reducing atmospheres[35] was developed and used in the 2nd generation cells. Furthermore, the WE design was adapted so that the topmost layer of this cell type is porous LSF, which enables operando investigation of the surface chemistry of LSF by APXPS measurements. In the APXPS analyzer, the atmospheric pressure and temperature are lower (1 mbar pressure, 600 °C) in order to meet the specifications of the APXPS setup.[38] WE and CE half-cell spectra collected within the APXPS chamber are shown in Figs. 10a–10b. The relatively low CE polarization resistance (green spectra) allows the acquisition of virtually artefact-free impedance spectra of the LSF electrode (blue arcs) in oxidizing and reducing conditions. Moreover, the WE overpotential could be determined with high precision. In oxidizing conditions, the WE half-cell spectrum appears larger than the full cell. This apparent error stems from the sequence of the individual measuremtns and the relatively fast degradation rate of the electrode in oxidizing atmosphere. Recently, atmospheric sulfur trace impurities were found to cause this fast initial degradation,[44] and a slight increase of the sulfur content with time was also observed during these APXPS measurements as well.

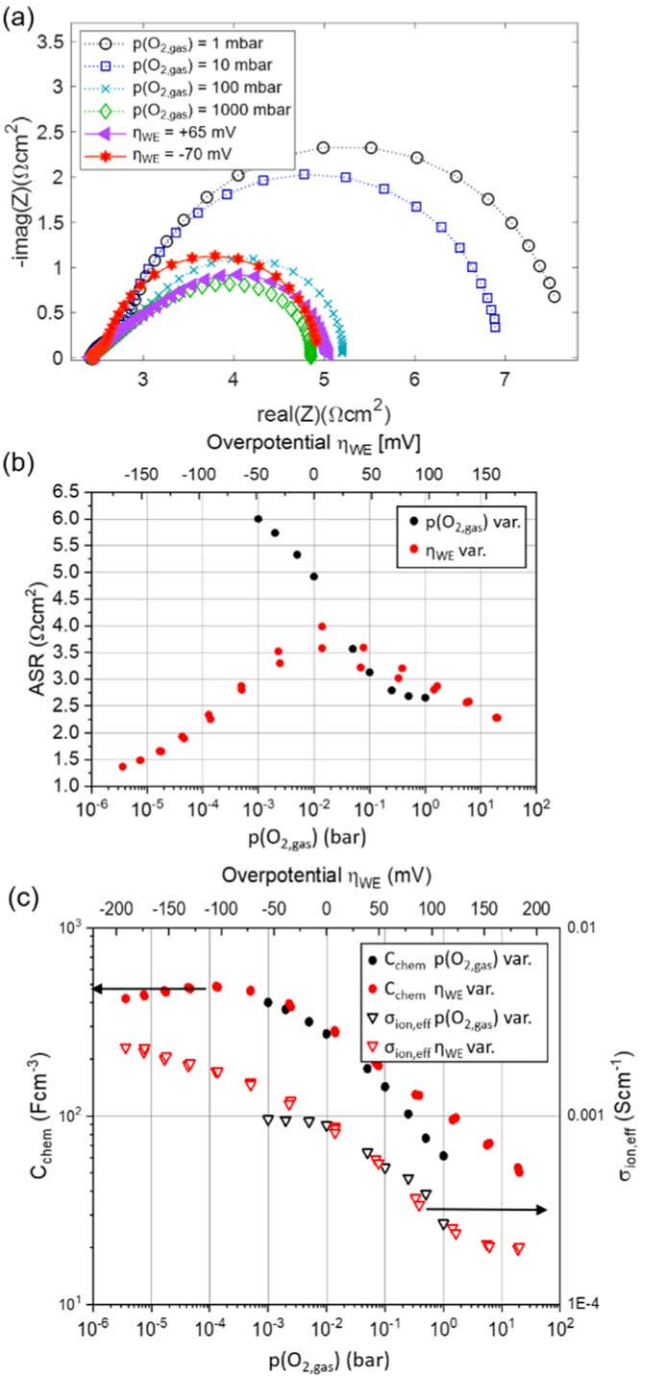

Figure 9. (a) Impedance spectra of the LSF half-cell at 700 °C collected at OCV and different $p(O_{2,gas})$ values, as well as varying overpotential (η_{WE}) at $p(O_{2,gas}) = 10$ mbar. (b) Area-specific resistance of the electrode as function of $p(O_{2,gas})$ variation (black circles) and WE overpotential variation at 10 mbar $p(O_{2,gas})$ (red circles). (c) Chemical capacitance (circles) and effective ionic conductivity (triangles) of the porous LSF electrode as a function of varying oxygen partial pressure at OCV (black symbols) and as a function of WE overpotential (red symbols) at 10 mbar $p(O_{2,gas})$.

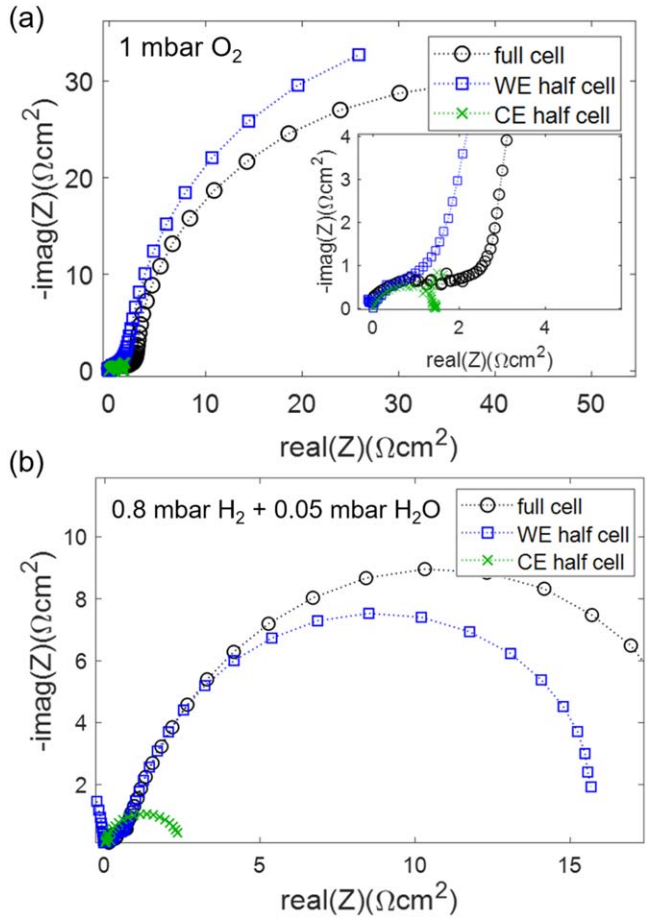

Figure 10. Impedance spectra of the three-electrode cell used for combined APXPS + EIS investigation, acquired in the APXPS chamber at 600 °C in (a) oxidizing and (b) reducing conditions.

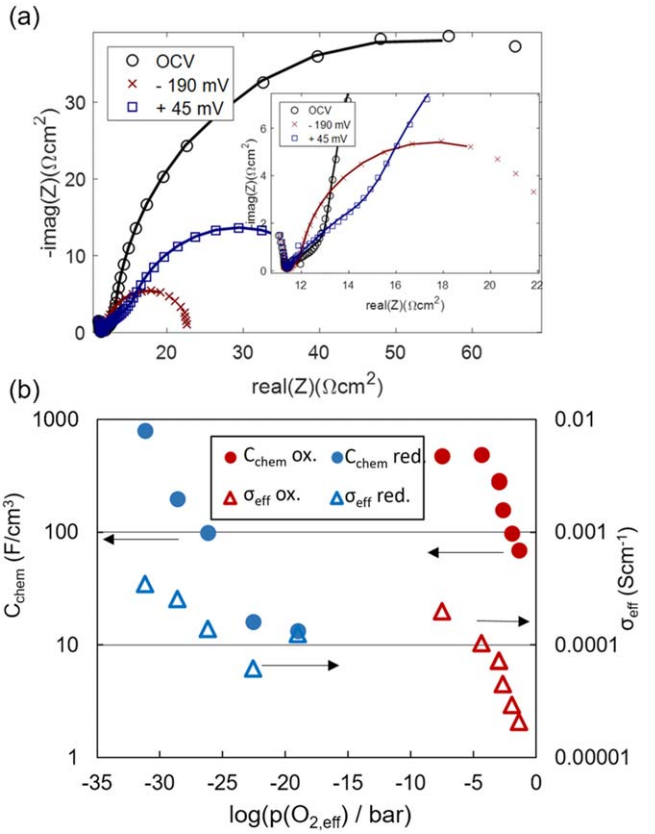

Figure 11. (a) Impedance spectra of the LSF half-cell at different overpotentials in 1 mbar O_2 (symbols) and fitting result (solid lines) and (b) fitted values for conductivity (triangles) and chemical capacitance (rectangles) as function of the effective $p(O_2)$.

The impedance spectra recorded at OCV and during electrochemical polarization in the APXPS chamber were fitted to the transmission line model shown in Fig. 6b, with the impedance function of Eq. 7, and a comparison of measured impedance spectra with their respective fit results are shown in Fig. 11a. Moreover, the obtained fitting parameters are plotted as function of $p(O_{2,eff})$ in Fig. 11b. In line with the defect chemical model of LSF[7,10,17] and the measurements shown in Fig. 9c, the chemical capacitance and effective ionic conductivity decrease sharply in the high $p(O_2)$ range, due to the decrease of the oxygen vacancy concentration. The chemical capacitance exhibits a complex $p(O_2)$ dependence with a maximum at ca 10^{-4} bar and a pronounced minimum close to the intrinsic point (10^{-18} bar) and increases again in more reducing conditions, due to the increase of the Fe^{2+} concentration. This is also predicted from the defect chemical model[7] shown in Fig. 1 and previous thin-film based measurements.[10,17]

The effective conductivity, on the other hand, also has a local minimum at 10^{-22} bar, rather than reaching a steady plateau value—although the oxygen vacancy concentration is relatively independent of the $p(O_2)$ between 10^{-5} and 10^{-25} bar. This at first sight surprising result is due to the placement of the electronic current collector in the 2nd generation cells, which sits below the electrode. The impedance function of this circuit does not depend individually on the resistances of electron and ion conduction, but only on the sum of both (Eq. 8), so the effective ambipolar conductivity $\sigma_{eff} = 1/(R_{ion} + R_{eon})$ is the proper fitting parameter. Consequently, the very low electronic conductivity close to the intrinsic point explains the local minimum of the ambipolar conductivity around 10^{-22} bars. Also the different location of local minima in C_{chem} and σ_{eff} on the $p(O_{2,eff})$ axis is reasonable, because the mobility of electron holes ($O_O^{\cdot}$) by far exceeds that of electrons (Fe'_{Fe}), so the conductivity minimum is shifted from the C_{chem} minimum at the intrinsic point where electrons and holes have equal concentrations.

Operando measurements of the LSF surface chemistry.— Simultaneous to the impedance measurements on cell type 2, ambient-pressure XPS measurements were carried out on the LSF electrode in order to link the surface chemistry and electrochemical properties at typical SOFC operating conditions under an applied bias voltage. From previous XPS and XAS studies of LSF thin films,[10,16,23,25] it is known that under sufficiently reducing conditions, metallic iron nanoparticles form at the surface and enhance the water splitting kinetics.[13,16]

The composition of the LSF surface measured by APXPS is given in Table I. In comparison to the nominal bulk composition ($La_{0.6}Sr_{0.4}FeO_{3-\delta}$), a strongly Sr enriched and Fe depleted surface is evident. A strong surface enrichment of A-site (especially Sr) cations is a typical phenomenon of perovskite-type electrodes.[12,45–47] Although the surface stoichiometry strongly deviates from the bulk, it remains quite stable during the measurements, even in dry H_2—where metallic Fe particles appear on the surface. In addition, minor impurities of S, Cr, Si and Pt were found on the surface. These elements were probably present in the sintering furnace atmosphere. The characteristic information depth of our XPS measurements is slightly smaller than the inelastic mean free path of 2.2 nm[48] for Sr3d photoelectrons, because most detected photoelectrons are not emitted perpendicular to the surface of the particles.

A main strength of the combined APXPS and electrochemical investigation is the possibility to directly observe the effect of electrochemical polarization and effective $p(O_2)$ on the oxygen exchange reaction kinetics, bulk defect chemistry and surface

Table I. Quantification of the surface chemistry of LSF in different atmospheres. Atomic concentrations were normalized to La+Sr+Fe = 100%.

	La 4d	Sr 3d	Fe 3p	O 1s	S 2p	Cr 2p	Si 2s	Pt 4f
1 mbar O_2	33	44	23	130	2.7	3.9	2.1	0.5
$H_2 + H_2O$	33	45	22	122	0.0	1.7	3.0	0.6
H_2 (dry)	32	47	21	129	0.0	2.0	—	—
Nominal	30	20	50	150	0	0	0	0

chemistry of the LSF layer. Application of an electrochemical overpotential or changing the atmosphere moves the position of the Fermi level within the band gap.[10,49,50] This in turn alters the measured binding energy of fixed-valent elements (e.g. La4d). The apparent binding energy in XPS is actually the energy difference between a core level electron and the Fermi level.[21,23,51] $E_b = E_f - E_{core}$. For LSF at p(O_2) values <1 mbar, the Fermi level lies within the bandgap. Therefore its position is related to the concentrations of n—and p-type defects according to

$$E_f = \frac{E_n + E_p}{2} + \frac{1}{2}k_b T \ln\left(\frac{[n]}{[p]}\right). \quad [11]$$

E_n and E_p are the energy levels of n—and p-type electronic defects in LSF, and [n] as well as [p] are their according concentrations. According to literature, the n-type defects are at Fe^{2+} polarons (Fe'_{Fe}),[7,10,52] and p-type defects have their main charge density at oxygen anions ($O_O^{\cdot}$).[23,53]

Below 1 mbar p(O_2), the electronic defect concentrations scale with [n] ~p(O_2)$^{-0.25}$ and [p] ~ p(O_2)$^{+0.25}$. When we insert these exponents into Eq. 11, we get

$$E_f = \frac{E_n + E_p}{2} + \frac{1}{4}k_b T \ln\left(\frac{p(O_{2,eff})}{p(O_{2,int})}\right). \quad [12]$$

Therein, p($O_{2,int}$) is the effective oxygen partial pressure at the intrinsic point where n and p-type defects have equal concentrations. This is at ca 10^{-18} bar, according to Fig. 1 - which coincides with the minimum in the chemical capacitance. In theory, the Fermi level (and hence the measured binding energy) should change with −43.5 mV dec^{-1} p($O_{2,eff}$). In Fig. 12 we show the binding energies of La4d and Fe2p peaks as function of p(O_2)$_{eff}$ to verify our model. The fitted slope for the La4d transition (−42 meV dec^{-1}) is excellently in line with the theory, whereas the slope for the Fe2p transition is slightly smaller with −30 meV dec^{-1}—the slightly shallower slope of the Fe2p BE is probably linked to the redox activity of Fe. It is worth emphasizing that measurements made in oxidizing and reducing conditions can be fitted with the same linear regression as shown in Fig. 12. Also the subtle flattening of the slopes above 1 mbar supports the model, because at higher p(O_2)$_{eff}$, the concentrations of electrons and holes become constant, see Fig. 1. This highlights that the effective oxygen partial pressure, given by Eq. 8 is an excellent descriptor for the Fermi level and the defect chemical state of the oxide.

Due to their localized nature,[53] electron holes should be observable in the XPS spectra. The O1s spectra shown in Fig. 13a contain three components. In literature, there is agreement that the black low BE component is related to a bulk species, and the other two components are enriched at the surface,[10,38,54] however there is no common agreement on the exact nature of the two surface components. The red component at ca 531.5 eV was recently shown to correspond to the presence of SO_4^{x-} groups.[38,44] Both the binding energy of sulfur peak shown in Fig. 13b, as well as the S 2p:O 1 s(SO_4) molar ratio of 3.5 ± 0.8 are well in line with this assignment. Most likely, atmospheric trace amounts of SO_2 are the source of this impurity, which vanishes in reducing conditions (probably due to the reduction of the SO_4^{2-} groups into gaseous H_2S).

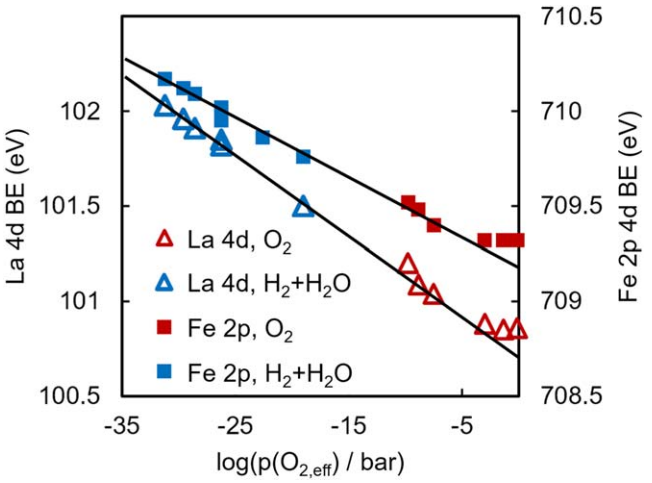

Figure 12. Binding energy of the La4d (triangles) and Fe2p (squares) main peaks in oxidizing (red) and reducing (blue) conditions. The black regression lines have a slope of −42 meV dec^{-1}. for the La4d peak and −30 meV dec^{-1}. for the Fe2p (oxide) peak.

Also the component at ca 530.5 eV is not agreed upon in literature. We tentatively assign this component to the presence of electron holes - which have predominant O 2p character,[23] and were previously shown to increase the O1s peak asymmetry.[21] In agreement with the defect chemical model of LSF, the "O 1 s polaron" component decreases in more reducing conditions (cathodic bias or $H_2 + H_2O$ atmospheres). Two models can explain this phenomenon: If holes are strongly localized as small polarons, this peak would correspond to a localized O^- species. Also when we assume less localized electron holes and a material with metallic electron structure, the hole-rich oxidized LSF would have metal-typical asymmerric peak shapes. Reduced LSF, which is a semi-conductor, in contrast has a slightly more symmetric O 1s peak.

The Fe2p spectra are more complex, and consist of two main peaks ($2p_{3/2}$ and $2p_{1/2}$) with a spin–orbit splitting of 13.5 eV—see Fig. 14. Each of these two peaks was fitted with two components (red and black curves in Fig. 14), which describe the complex, asymmetric shape of the Fe oxide peaks and do not represent different chemical states. The spin–orbit doublet was constrained to equal FWHM, 1:2 area ratio and 13.5 eV energy difference. A broad satellite feature (Fe^{3+} sat) is also present at a binding energy of ca 719 eV, which is characteristic for Fe^{3+}.[55,56] Fe oxidation states are not trivial to quantify, and the most pronounced changes are not found in the main peaks, but in the satellite features.[55,57] Fe^{3+} compounds have a satellite feature at 718–719 eV, whereas Fe^{2+} compounds have the satellite at 714–715 eV. In some literature, the electron hole is assumed to be located at Fe^{4+} states,[7,20] but neither our measurements nor previous studies[23] found spectroscopic evidence for this hypothesis. Hence, our results confirm the location of the electron hole in O2p-like states. In reducing conditions, ferrite-perovskites become n-type conductive and the electronic defect is strongly localized to Fe^{2+} ions.[7,10,51] On the porous electrodes, however we do not observe a clear Fe^{2+} satellite feature, although a Fe^{2+} fraction up to approx. 20% at the surface may be present but remain undetected due to the relatively weak and broad

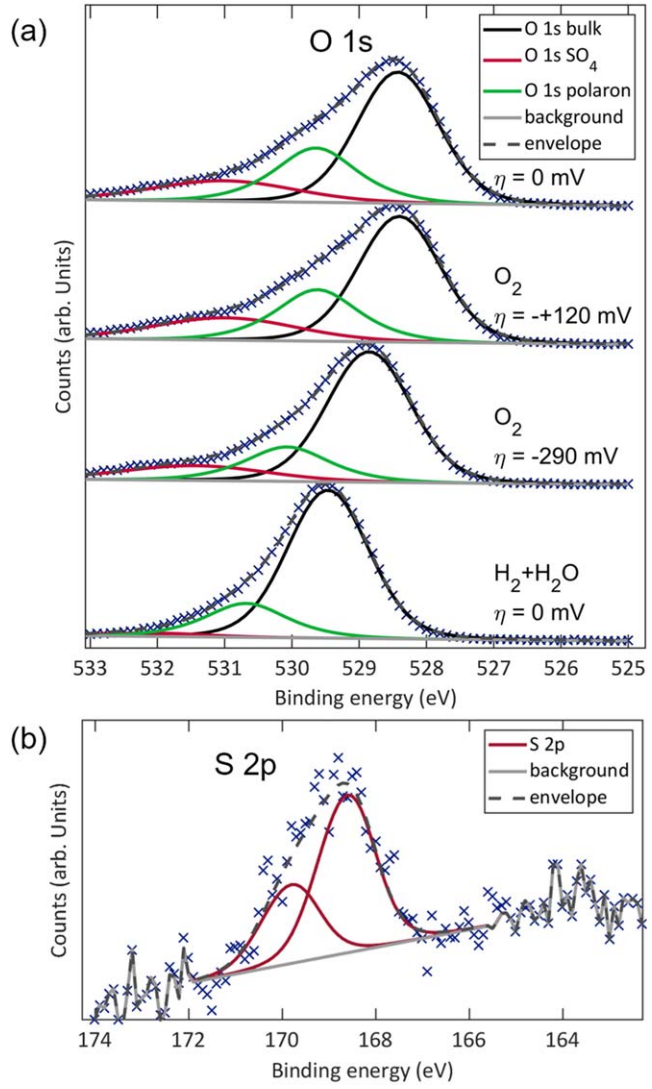

Figure 13. (a) O 1 s spectra of LSF at different overpotentials in O_2 and $H_2 + H_2O$ atmospheres at 600 °C. The SO_4 component was assigned due to the presence of a sulfur species in oxidizing conditions (plot part b).

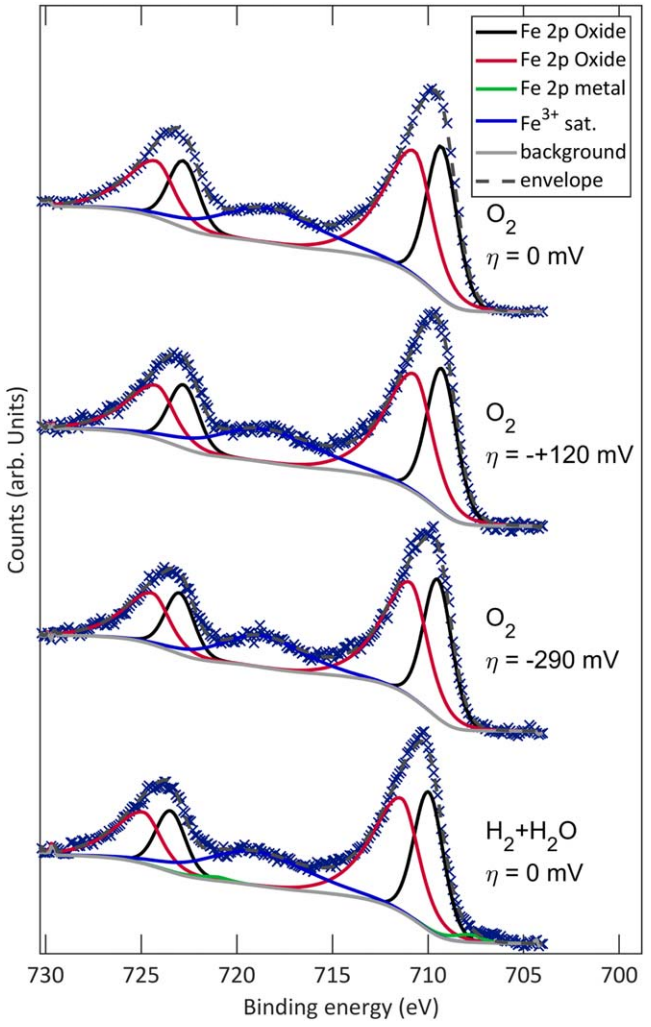

Figure 14. Fe2p spectra of LSF acquired at different overpotentials in O_2 and $H_2 + H_2O$ atmospheres at 600 °C.

nature of the satellite features. In previous synchrotron-based studies on LSF thin films, Fe^{2+} and Fe^{3+} oxidation states were detected in similar amounts,[10,51] but it has to be considered that the photon energy and hence XPS probing depth in these studies was much lower than in the present work. However, we do observe an additional very small peak in $H_2 + H_2O$ atmosphere at 707 eV, which is characteristic for metallic iron, and was observed before[13,25,51] also on LSF thin films.

Enhancement of water splitting kinetics by Fe^0 nanoparticles.—The presence of exsolved metallic nanoparticles on the surface is quite relevant for the usage of LSF as a steam electrolysis cathode, because previous studies have shown strongly enhanced (electro)chemical kinetics on perovskite-type electrodes with exsolved metallic nanoparticles,[25,58–62] including LSF.[13,16,63] For better visibility of the Fe meal peak, a magnification of this region in O_2 atmosphere and different reducing conditions is shown in Fig. 15. The blue numbers correspond to the experimental measurement sequence number, which is also shown in Fig. 16a. The conditions at which Fe metal appears are well in line with literature APXPS studies on LSF thin films,[13,25,63] and are furthermore in agreement with thermogravimetric measurements of LSF powder.[7]

In Fig. 16a, the percentage of metallic Fe^0 is plotted vs overpotential (blue diamond symbols). Clearly visible, the Fe^0 fraction increases when cathodic bias is applied. However, the kinetics of nanoparticle formation and growth depend in a complex manner on the overpotential, atmosphere, temperature and time.[59,64] Therefore, all measurements of the Fe^0 fraction are numbered, according to the sequence in which they were measured (ca. 30 min pass between two experimental points). After variation of the bias, the Fe^0 fraction was measured as a function of time in pure H_2 atmosphere (black diamond symbols in Fig. 15a). Clearly visible, the Fe^0 fraction gradually increases, indicating that LSF is not thermodynamically stable in dry H_2 atmosphere, as suggested from previous thermogravimetric studies.[7]

Moreover, the strongly promoting effect of exsolved Fe^0 metal particles on the water-splitting kinetics is visible in the current-voltage curve shown in Fig. 16a (black hollow squares). The much steeper cathodic I–V branch coincides with an increased Fe^0 fraction, which indicates that the reversible oxidation and reduction of Fe nanoparticles is the reason for the enhanced water splitting activity. The strong catalytic effect of the Fe^0 nanoparticles is even more pronounced in the impedance spectra shown in Fig. 16b. At +157 mV overpotential—which is sufficient to oxidize Fe nanoparticles to iron oxides, the polarization resistance is 4 times larger than at open circuit conditions, whereas the arc shrinks from 20 to 2 Ωcm^2 when an overpotential of just −100 mV is applied, and more Fe^0 is present at the surface. In terms of amount, about 10%–15% of

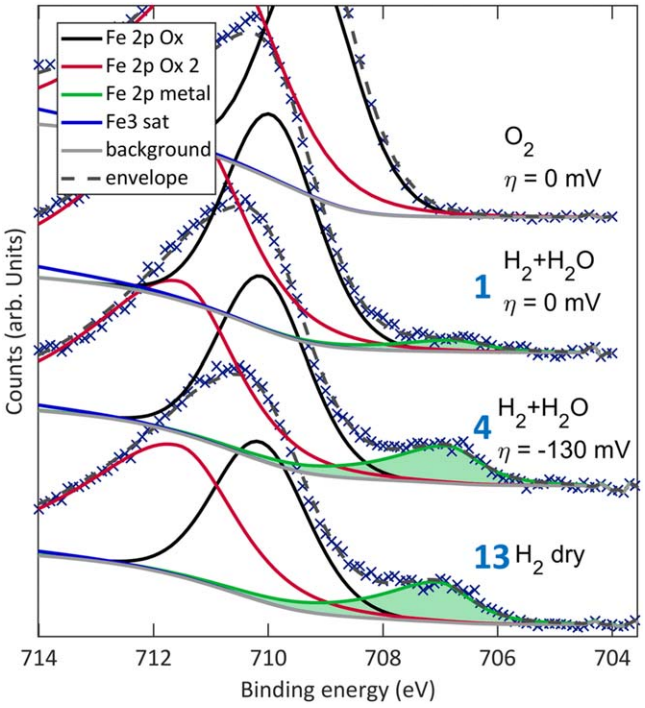

Figure 15. Magnification of the Fe 2p metal peak (green) in different reducing conditions. The blue numbers correspond to the sequence number that is also shown in Fig. 16a.

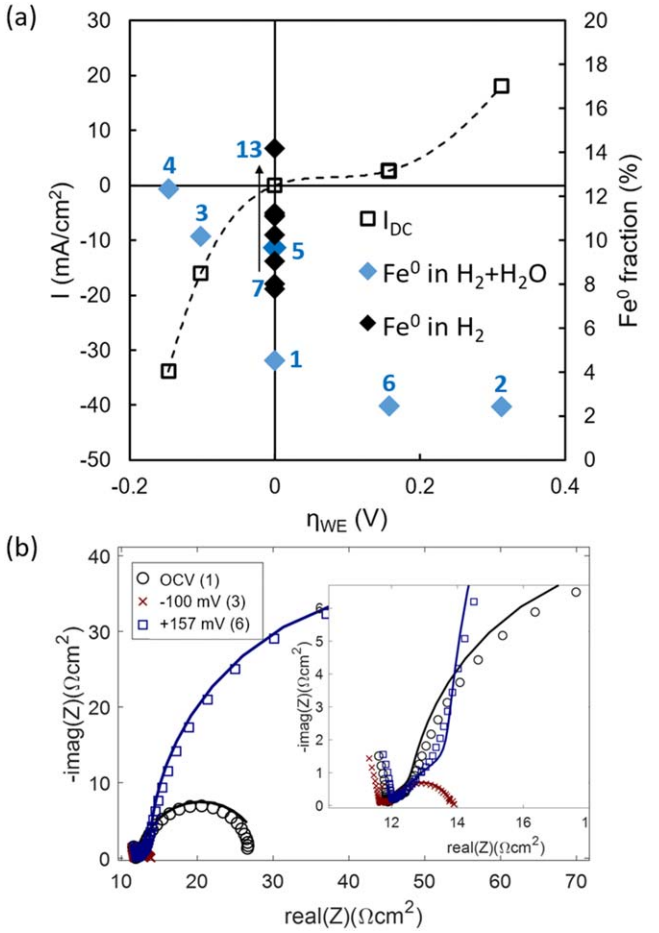

Figure 16. (a) Fe^0 fraction (% of total Fe) of the LSF electrode in reducing atmosphere, as function of the electrode overpotential in $H_2 + H_2O$ (blue rhombus), as well as at OCV in pure H_2 atmosphere (black rhombus). The numbers 1–13 represent the order in which the spectra were acquired. Open squares represent the current-voltage characteristics; the dashed line is a guide for the eye. (b) Impedance spectra (symbols) and transmission line fit (lines) of the LSF half-cell at different overpotential. The spectrum at −100 mV overpotential is only visible in the inset.

the measurable Fe atoms are metallic, and 22% of the surface cations are Fe, so the Fe particle surface coverage is merely 2%–3%. On a pure oxide electrode, the formation of H_2 from two surface OH groups is believed to be the rate-limiting step in high temperature electrolysis,[50,65] as well as photochemical water splitting.[66,67] After Fe^0 exsolution, surface hydrogen may diffuse onto the metallic nanoparticles on which the H_2 release reaction is much faster.[13,50] Consequently, the activity is expected to scale with the triple-phase boundary density of the Fe^0 particles on LSF, which is quite large on electrodes with nanoparticle exsolutions, compared to classical cermet electrodes with micrometre sized metal particles.

Conclusions and Outlook

In this study, we presented a new three-electrode cell design for solid electrolytes, which minimizes the artefacts that often occur in this type of measurements utilizing a reference electrode. Moreover, the model cell has a porous working electrode with an embedded thin film current collector, which allows the operando investigation of the working electrode functional layer by ambient pressure XPS (APXPS). With such a cell, we simultaneously investigated the electrochemical and surface chemical properties of porous LSF electrodes in oxidizing and reducing atmospheres during application of an overpotential. From these measurements, we could draw several important conclusions:

1. With the proper selection of electrode materials, it is possible to measure virtually artefact-free half-cell impedance spectra and accurately determine the overpotentials of single electrodes.
2. The optimal choice of WE and CE materials requires different summit frequencies of the two electrodes and the counter electrode polarization resistance must be similar to or smaller than that of the working electrode. Then, possible artefact features are small and can be clearly identified by their frequency, which matches that of the counter electrode.
3. The impedance spectra of LSF electrodes were fitted to a transmission line equivalent circuit model, which models the processes of oxide ion conduction, surface oxygen exchange reaction and changes in oxygen stoichiometry through the chemical capacitance. We could show that electrochemical polarization and $p(O_2)$ variations affect the bulk parameters oxide ion conductivity and chemical capacitance in the same manner in accordance with Nernst's equation, which is applicable for a rate-limiting surface oxygen exchange reaction. The electrochemical properties behave as expected from bulk defect chemical investigations.
4. The surface chemistry of the LSF working electrode is strongly Sr-enriched, but compositionally very stable during electrochemical polarization and atmosphere switching. The measurements also revealed that the Fermi level varies systematically with the effective oxygen partial pressure in the MIEC material, and can be tracked by binding energy changes of fixed-valent elements (e.g. La 4d).
5. Changes of the effective $p(O_2)$ by atmosphere and bias variation affect the oxygen vacancy concentration, which is balanced by electron holes with predominant O2p character at high pO_2, and changes of Fe oxidation states in reducing conditions. In strongly reducing conditions, metallic Fe^0 appears on the LSF surface and has a strongly promoting effect on the electrochemical water splitting kinetics.

In summary, our combined operando APXPS + EIS technique delivered new insight into the mechanisms of oxygen exchange and surface chemistry of 3D porous LSF electrodes, and the results are

well in line with previous studies on model-type LSF thin films. The results show the strength of the used experimental approach to identify electrochemical oxygen exchange mechanisms and to better understand the link between surface chemistry and electrochemical properties. LSF serves as a model material due to its well-investigated defect chemistry, but the novel cell geometry is of course excellently suited to study also other electrode materials (e.g. LSCF, LSM-YSZ, ceria-based anodes).

Acknowledgments

We thank Alexander Schmid for the permission to reproduce Fig. 1 in this publication and Joseph Ring for SEM operation.

This research was partially funded by the European Research Council (ERC) under the European Union's Horizon 2020 research and innovation programme, grant agreement no. 755744/ERC—Starting Grant TUCAS.

ORCID

Andreas Nenning https://orcid.org/0000-0001-9313-3731
Richard Schlesinger https://orcid.org/0000-0002-2143-185X
Lorenz Lindenthal https://orcid.org/0000-0002-2768-6079
Tobias M. Huber https://orcid.org/0000-0001-6339-8341
Christoph Rameshan https://orcid.org/0000-0002-6340-4147
Jürgen Fleig https://orcid.org/0000-0002-8401-6717
Alexander K. Opitz https://orcid.org/0000-0002-2567-1885

References

1. A. Nenning, C. Bischof, J. Fleig, M. Bram, and A. K. Opitz, *Energies*, **13**, 987 (2020).
2. S. B. Adler, J. A. Lane, and B. C. H. Steele, *J. Electrochem. Soc.*, **143**, 3554 (1996).
3. S. McIntosh, S. B. Adler, J. M. Vohs, and R. J. Gorte, *Electrochem. Solid-State Lett.*, **7**, A111 (2004).
4. F. Han, R. Mücke, T. Van Gestel, A. Leonide, N. H. Menzler, H. P. Buchkremer, and D. Stöver, *J. Power Sources*, **218**, 157 (2012).
5. S. Dierickx, T. Mundloch, A. Weber, and E. Ivers-Tiffée, *J. Power Sources*, **415**, 69 (2019).
6. A. Leonide, Y. Apel, and E. Ivers-Tiffee, *ECS Trans.*, **19**, 81 (2009).
7. M. Kuhn, S. Hashimoto, K. Sato, K. Yashiro, and J. Mizusaki, *Solid State Ion.*, **195**, 7 (2011).
8. A. Schmid, G. M. Rupp, C. Slouka, E. Navickas, L. Andrejs, H. Hutter, L. Volgger, A. Nenning, and J. Fleig, *Acta Chim. Slov.*, **63**, 509 (2016).
9. A. Schmid, G. M. Rupp, and J. Fleig, *Chem. Mater.*, **30**, 4242 (2018).
10. A. Nenning, A. K. Opitz, C. Rameshan, R. Rameshan, R. Blume, M. Hävecker, A. Knop-Gericke, G. Rupprechter, B. Klötzer, and J. Fleig, *J. Phys. Chem. C*, **120**, 1461 (2016).
11. S. Kogler, A. Nenning, G. M. Rupp, A. K. Opitz, and J. Fleig, *J. Electrochem. Soc.*, **162**, F317 (2015).
12. C. Riedl, A. Schmid, A. Nenning, H. Summerer, S. Smetaczek, S. Schwarz, J. Bernardi, A. Optiz, A. Limbeck, and J. Fleig, *J. Electrochem. Soc.*, **167**, 104514 (2020).
13. A. K. Opitz et al., *Nat. Commun.*, **11**, 4801 (2020).
14. F. S. Baumann, J. Maier, and J. Fleig, *Solid State Ion.*, **179**, 1198 (2008).
15. F. S. Baumann, J. Fleig, G. Cristiani, B. Stuhlhofer, H. U. Habermeier, and J. Maier, *J. Electrochem. Soc.*, **154**, B931 (2007).
16. A. K. Opitz, A. Nenning, C. Rameshan, R. Rameshan, R. Blume, M. Hävecker, A. Knop-Gericke, G. Rupprechter, J. Fleig, and B. Klötzer, *Angew. Chem. Int. Ed.*, **54**, 2628 (2014).
17. A. Schmid, G. M. Rupp, and J. Fleig, *Phys. Chem. Chem. Phys.*, **20**, 12016 (2018).
18. F. A. Kröger and H. J. Vink, *Solid State Phys.*, ed. F. Seitz and D. Turnbull (Academic, New York, NY) 3, p. 307 (1956), https://www.sciencedirect.com/science/article/pii/S0081194708601356.
19. H. Ullmann, N. Trofimenko, F. Tietz, D. Stöver, and A. Ahmad-Khanlou, *Solid State Ion.*, **138**, 79 (2000).
20. M. Søgaard, P. Vang Hendriksen, and M. Mogensen, *J. Solid State Chem.*, **180**, 1489 (2007).
21. H. Wadati et al., *Phys. Rev. B*, **71**, 035108 (2005).
22. C. Franchini, M. Reticcioli, M. Setvin, and U. Diebold, *Nat. Rev. Mater.*, **6**, 560 (2021).
23. D. N. Mueller, M. L. Machala, H. Bluhm, and W. C. Chueh, *Nat. Commun.*, **6** (2015).
24. K. Syed, J. Wang, B. Yildiz, and W. J. Bowman, *Nanoscale*, **14**, 663 (2022).
25. J. Wang et al., *Chem. Mater.*, **33**, 5021 (2021).
26. J. Costard, M. Ender, M. Weiss, and E. Ivers-Tiffée, *J. Electrochem. Soc.*, **164**, A80 (2016).
27. S. Solchenbach, D. Pritzl, E. J. Y. Kong, J. Landesfeind, and H. A. Gasteiger, *J. Electrochem. Soc.*, **163**, A2265 (2016).
28. S. B. Adler, *J. Electrochem. Soc.*, **149**, E166 (2002).
29. M. Cimenti, V. I. Birss, and J. M. Hill, *Fuel Cells*, **7**, 377 (2007).
30. M. Cimenti, A. C. Co, V. I. Birss, and J. M. Hill, *Fuel Cells*, **7**, 364 (2007).
31. J. Winkler, P. V. Hendriksen, N. Bonanos, and M. Mogensen, *J. Electrochem. Soc.*, **145**, 1184 (1998).
32. S. J. Kim, K. J. Kim, and G. M. Choi, *Int. J. Hydrog. Energy*, **40**, 9032 (2015).
33. M. K. Stodolny, B. A. Boukamp, D. H. A. Blank, and F. P. F. van Berkel, *J. Power Sources*, **209**, 120 (2012).
34. R. Schlesinger, *Thesis*, TU Wien (2018), Vienna https://publik.tuwien.ac.at/files/publik_270965.pdf.
35. A. Nenning, M. Holzmann, J. Fleig, and A. K. Opitz, *Mater. Adv.*, **2**, 5422 (2021) https://pubs.rsc.org/en/content/articlelanding/2021/ma/d1ma00202c.
36. M. Gerstl, A. Nenning, R. Iskandar, V. Rojek-Woeckner, M. Bram, H. Hutter, and A. K. Opitz, *Materials*, **9**, 649 (2016).
37. J. Bisquert, *Phys. Chem. Chem. Phys.*, **2**, 4185 (2000).
38. R. Rameshan, A. Nenning, J. Raschhofer, L. Lindenthal, T. Ruh, H. Summerer, A. K. Opitz, T. M. Huber, and C. Rameshan, *Crystals*, **10**, 947 (2020).
39. C. Ahamer, A. K. Opitz, G. M. Rupp, and J. Fleig, *J. Electrochem. Soc.*, **164**, F790 (2017).
40. S. Reuter, "Three-electrode measurements in solid oxide fuel cell research." *Wien* (2020).
41. J. Jamnik and J. Maier, *Phys. Chem. Chem. Phys.*, **3**, 1668 (2001).
42. A. Nenning, M. Gerstl, M. Bram, and A. K. Opitz, *ECS Trans.*, **91**, 479 (2019).
43. B. Hirschorn, M. E. Orazem, B. Tribollet, V. Vivier, I. Frateur, and M. Musiani, *Electrochim. Acta*, **55**, 6218 (2010).
44. A. Schmid, A. Nenning, A. Opitz, M. Kubicek, and J. Fleig, *J. Electrochem. Soc.*, **167**, 124509 (2020).
45. W. Jung and H. L. Tuller, *Energy Environ. Sci.*, **5**, 5370 (2012).
46. G. M. Rupp, A. K. Opitz, A. Nenning, A. Limbeck, and J. Fleig, *Nat. Mater.*, **16**, 640 (2017).
47. A. K. Opitz et al., *Top. Catal.*, **61**, 2129 (2018).
48. S. Tanuma, C. J. Powell, and D. R. Penn, *Surf. Interface Anal.*, **35**, 268 (2003).
49. C. Zhang, M. E. Grass, Y. Yu, K. J. Gaskell, S. C. DeCaluwe, R. Chang, G. S. Jackson, Z. Hussain, H. Bluhm, and B. W. Eichhorn, *ACS Catal.*, **2**, 2297 (2012).
50. Z. A. Feng, F. El Gabaly, X. Ye, Z.-X. Shen, and W. C. Chueh, *Nat. Commun.*, **5**, 4374 (2014).
51. A. Nenning and J. Fleig, *Surf. Sci.*, **680**, 43 (2019).
52. A. Nenning, L. Volgger, E. Miller, L. V. Mogni, S. Barnett, and J. Fleig, *J. Electrochem. Soc.*, **164**, F364 (2017).
53. C. Hartmann, J. Laurencin, and G. Geneste, *ECS Trans.*, **103**, 1491 (2021).
54. E. J. Crumlin, E. Mutoro, W. T. Hong, M. D. Biegalski, H. M. Christen, Z. Liu, H. Bluhm, and Y. Shao-Horn, *J. Phys. Chem. C*, **117**, 16087 (2013).
55. M. Descostes, F. Mercier, N. Thromat, C. Beaucaire, and M. Gautier-Soyer, *Appl. Surf. Sci.*, **165**, 288 (2000).
56. M. C. Biesinger, B. P. Payne, A. P. Grosvenor, L. W. M. Lau, and A. R. Gerson, "and R. St. C. Smart." *Appl. Surf. Sci.*, **257**, 2717 (2011).
57. T. Yamashita and P. Hayes, *Appl. Surf. Sci.*, **254**, 2441 (2008).
58. T. Zhu, H. E. Troiani, L. V. Mogni, M. Han, and S. A. Barnett, *Joule*, **2**, 478 (2018).
59. D. Neagu et al., *ACS Nano*, **13**, 12996 (2019).
60. D. Neagu, T.-S. Oh, D. N. Miller, H. Ménard, S. M. Bukhari, S. R. Gamble, R. J. Gorte, J. M. Vohs, and J. T. S. Irvine, *Nat. Commun.*, **6**, 1 (2015).
61. H. Han, J. Park, S. Y. Nam, K. J. Kim, G. M. Choi, S. S. P. Parkin, H. M. Jang, and J. T. S. Irvine, *Nat. Commun.*, **10**, 1 (2019).
62. L. Lindenthal, J. Huber, H. Drexler, T. Ruh, R. Rameshan, F. Schrenk, S. Löffler, and C. Rameshan, *Catalysts*, **11**, 1484 (2021).
63. L. Lindenthal, R. Rameshan, H. Summerer, T. Ruh, J. Popovic, A. Nenning, S. Löffler, A. K. Opitz, P. Blaha, and C. Rameshan, *Catalysts*, **10**, 268 (2020).
64. J. K. Kim, Y.-R. Jo, S. Kim, B. Koo, J. H. Kim, B.-J. Kim, and W. Jung, *ACS Appl. Mater. Interfaces*, **12**, 0c05215 (2020).
65. A. Nenning, E. Navickas, H. Hutter, and J. Fleig, *J. Phys. Chem. Lett.*, **7**, 2826 (2016).
66. J. B. Joo, R. Dillon, I. Lee, Y. Yin, C. J. Bardeen, and F. Zaera, *Proc. Natl Acad. Sci.*, **111**, 7942 (2014).
67. C. A. Walenta, C. Courtois, S. L. Kollmannsberger, M. Eder, M. Tschurl, and U. Heiz, *ACS Catal.*, **10**, 4080 (2020).